Journal of Environmental Analysis and Progress

ISSN: 2525-815X

10.24221/jeap.9.4.2024.7364.340-355

X-ray computed tomography for estimating density and porosity in reservoir analogous rocks: a study on laminated limestones from the Crato Formation

Frederico Veiga Ribeiro Gonçalves[a], Daniel Milian Pérez[a], Abel Gámez Rodríguez[a], Yaicel Ge Proenza[a], Daniel Amancio Duarte[a], Márcio Fernando Paixão de Brito[a], Cássia Bezerra Machado[a], Raquel Milani[a], Daiane Francisca do Nascimento Silva[a], Frederico Dias Nunes[a], Jose Antonio Barbosa[b], Igor Fernandes Gomes[c], Antonio Celso Dantas Antonino[a]

[a] Universidade Federal de Pernambuco-UFPE, Departamento de Energia Nuclear. Av. Professor Luiz Freire, n. 1000, Cidade Universitária, Recife, Pernambuco, Brasil. CEP: 50.740-545. E-mail: frederico.goncalves@ufpe.br, daniel.milian@ufpe.br, abel.rodriguez@ufpe.br, yaicel.geproenza@ufpe.br, daniel.aduarte@ufpe.br, marcio.paixao@ufpe.br, cassia.bezerra@ufpe.br, raquel.milani@ufpe.br, daiane.francisca@ufpe.br, frederico.nunes@ufpe.br, antonio.antonino@ufpe.br.

[b] UFPE, Departamento de Geologia. Avenida Arquitetura, n. 100, Cidade Universitária, Recife, Pernambuco, Brasil. CEP: 50.740-550. E-mail: jose.antoniob@ufpe.br.

[c] UFPE, Departamento de Engenharia Civil. Avenida Arquitetura, n. 100, Cidade Universitária, Recife, Pernambuco, Brasil. CEP: 50.740-550. E-mail: igor.fernandes@ufpe.br.

ARTICLE INFO

Received 28 Sep 2024
Accepted 04 Dec 2024
Published 16 Dec 2024

ABSTRACT

In recent decades, faster and more affordable methods for characterizing reservoir rocks in environmental and geological studies have gained importance, particularly for hydrocarbon exploration and resource management. One promising method is X-Ray Computed Micro-Tomography (XR-µCT), enabling non-destructive analysis of rock properties. However, this technique presents challenges related to image interpretation, property characterization below the voxel scale, and results in comparison across configurations. This study analyzed laminated limestones from the Crato Formation, analogs to the pre-salt Barra Velha Formation, using XR-µCT to estimate density and porosity. These rocks are substitutes for actual reservoir conditions, addressing the challenge of limited subsurface samples. This study assessed the feasibility of XR-µCT for characterizing these properties and understanding the impact of millimeter-scale laminations on their distribution. Calibration values for calcite, the primary mineral, were used to ensure accuracy and repeatability. The results demonstrate that XR-µCT is a viable environmental and geological characterization tool. Laminations due to stratification influenced porosity distribution in the axial direction, with higher concentrations in certain sections of the samples. The porosity values calculated using XR-µCT align relatively well with the gas porosimetry results, with most samples showing a relative difference of less than 10%. However, exceptions were observed in LM4 and T10.2, where the relative difference reached -15.90% and -12.80%, respectively. Despite these challenges, qualitative analysis was achieved. The study highlights the necessity of accounting for mineralogy and calibration in XR-µCT to ensure reliable comparisons across different tomographic systems, enhancing the method's applicability in environmental and geological studies.

Keywords: X-ray computed tomography, laminated carbonate, Crato Formation, density, porosity.

Introduction

The pre-salt is a rock formation located underground on the Brazilian coast, approximately 300 kilometers offshore, which extends between the states of Santa Catarina and Espírito Santo, reaching an area of around 800 kilometers long and 200 kilometers wide (Dou et al., 2024; Hai et al., 2024; Rossoni et al., 2024). This rock formation is the most significant oil discovery in the past five decades. Brazilian reserve estimates indicate up to 15 billion barrels of recoverable oil equivalent, comprising 12.8 billion barrels of oil and 380

billion cubic meters of natural gas. The pre-salt represents more than half (56%) of the national reserves (Abelha & Petersohn, 2019). However, the exact amount of oil in the pre-salt is still unknown, as some studies suggest that the actual reserves might be up to twice as much as those currently projected. These reserves are located below the seabed, in the deep and ultra-deep waters of the Santos and Campos Basins, and beneath rock layers that are 3 to 4 kilometers thick. This set of rocks, with potential for the formation of oil, is located under an extensive layer of salt that reaches thicknesses of up to two thousand meters, forming a kind of seal and thus guaranteeing the generation of excellent quality oil (Neves Junior et al., 2023; Pilotto et al., 2024).

The study of properties and characterization of rocks in the limestone reservoirs of Brazil's pre-salt region is crucial for the efficient and safe exploration of these extensive oil reserves. To this end, efforts have been focused on characterizing reservoir rocks and their analogs, particularly geological facies that pose challenges in the assessment and exploitation of energy resources (Busch et al., 2022; Alencar et al., 2024; Michael, 2024; Valencia-Gómez et al., 2024). In literature, a substantial number of articles with this focus have been identified using various methods. One such method that has been successfully used in recent years for the study of the properties and characterization of reservoir rocks is the X-Ray Computed micro-Tomography (XR-μCT) (Xie et al., 2022; Pak et al., 2023; Q. Liu et al., 2023; Shukla et al., 2024). This technique offers advantages over others as it allows for a quantitative, three-dimensional representation of the microstructure of porous geomaterials and directly measures the complex morphology of the pore space in sedimentary rocks at resolutions that can reach a few micrometers. Additionally, it is a fast and non-invasive technique that provides quantitative results on the mineralogy and pore space of rocks and can be used for petrophysical, mechanical, and flow studies. The image generated by this method depends on the rock's density and effective atomic number (mineralogy). Depending on the scale used, 3D image analysis can estimate density and porosity, fracture patterns, quantify mineralogies, and complex microstructures. Combined with the rock's macrostructure, these factors allow for predictions about reserve volume and production estimates, contributing to a more accurate interpretation of the reservoirs. Finally, the development of this technique, as well as the evolution of computational methods, have made it possible to replace synthetic images derived from statistical models obtained from 2D images with three-dimensional representations of the pore space in rocks (Wellington & Vinegar, 1987; Cnudde & Boone, 2013; Zhu et al., 2018; Lv et al., 2020; Wang et al., 2021).

For example, Teles et al. (2016) evaluated the pore space evolution of a rock sample retrieved from the coquina region of the subterranean pre-salt carbonate reservoir formation subjected to a hydrochloric acid flow through the whole sample. For that, they employed X-Ray Computed Tomography with a microfocus source. This research allowed, for the first time, a visual investigation of the consequences of an acid system on subterranean pre-salt carbonate reservoir outcrops. The findings revealed that the branches of the wormhole deviate from the areas close to the main channel, and the quartz volume diminishes following acid treatment. It was confirmed that while the acid primarily interacts with the most porous areas, the wormhole also traverses zones of lower porosity. This process results in an overall increase in the porosity of the carbonate rock. Additionally, Islam et al. (2018) presented insights into the processes of imaging, segmentation, and numerical simulation of single-phase flow through both a standard homogeneous Silurian dolomite core plug sample and a heterogeneous sample from a carbonate reservoir. XR-μCT was performed using a Versa 500 CT device. They also developed a procedure incorporating experimental results into the segmentation phase to calibrate porosity and utilized two different numerical tools for simulating fluid flow. Furthermore, Herlinger & Vidal (2022) aimed to understand and predict Sor in pre-salt carbonates of the Barra Velha Formation, Santos Basin, using Ensemble Learning techniques (AdaBoost, Gradient Boost, and XGBoost) with X-ray μCT scans and routine core analysis (RCAL) data. They extracted morphological attributes related to pore size, shape, and orientation from the scans to build machine-learning models. Their findings showed that facies control significantly affected Sor due to rock genesis variations. Larger pores led to more heterogeneity and oil trapping. Gradient Boosting performed best, and RCAL data did not improve model accuracy, indicating Sor could be predicted using only morphological attributes. Moreover, Liu et al. (2023) employed XR-μCT to reconstruct the 3D pore space of selected samples from unconventional volcanic reservoirs in the Songliao Basin (NE China) at depths between 2283 and 3757 meters. They reconstructed the morphology and size distribution of the pores in selected samples of basaltic lava, rhyolitic lava, and rhyolitic pyroclastics. Their study investigated potential relationships between porosity and permeability

but found no clear correlation between these parameters or depth and permeability. Although their analysis is valid within a length scale of about 20 µm to 1 cm, their methodological approach can be extended to other reservoirs to study the evolution of pore systems as a function of various processes affecting volcanic rocks. Lastly, Martyushev et al. (2023) applied thin sections and computed tomography to analyze the petrography, 2D pore images, and 3D pore network of carbonate reservoirs from three oil fields in Perm Krai, Russia. Well-testing and core studies revealed detailed structural features of the reservoirs, showing that magnesium in the limestone reduced its capacitive characteristics. They identified three types of void spaces: (i) primary intercrystalline pores, (ii) larger secondary pores, and (iii) a combination of primary and secondary voids connected by partially healed fractures. These structural variations affect reservoir behavior, with larger voids and higher initial permeability leading to intense deformation and decreased permeability as pressure drops. Finally, Kadyrov et al. (2024) explored the integration of high-resolution XR-µCT imaging and transfer learning for the automated characterization of reservoir rocks and tomofacies identification. Their study employed a dataset of 66,560 2D µCT images of 130 standard core plugs, encompassing all major reservoir rock types, for model training. The effectiveness of the transfer learning for rock characterization achieved high validation rates, with an average classification accuracy of over 94%. This hints that integrating XR-µCT imaging and transfer learning could improve reservoir rock characterization's automation, speed, and accuracy.

As observed, many of these studies using XR-µCT to characterize reservoir rocks employ standard segmentation techniques based on obtaining a threshold value to differentiate the solid matrix from the void space. However, some of the reservoir rocks in the pre-salt, such as the laminated limestones found in certain formations of the Santos Basin, have their porous space constituted by pores with dimensions below 10 µm or even at the nanometric scale. In this pore size range, it is impossible to capture the details of the full core plug sample microstructure at the standard resolution of most commercially available µCT scanners, which have a voxel size of ~20-40 µm3. Therefore, for these rock samples, standard segmentation techniques that implement a threshold value are not adequate. This is precisely one of the challenges of XR-µCT: the interpretation of images and characterization of properties below the voxel scale.

This study aimed to develop, apply, and validate an analogous method for characterizing properties in laminated limestones with a porous microstructure below the µCT voxel scale. The strength of this method lies in its ability to quickly provide estimates consistent with those obtained by traditional petrophysical methods for the same lithology, specifically regarding the density and porosity of the lithological features of interest.

Material and Methods

This study focused on characterizing the laminated deposits that comprise some facies of the pre-salt interval reservoirs in the Santos Basin, specifically the laminates of the Barra Velha Formation. The Barra Velha Formation in the Santos Basin (Figure 1) is a major pre-salt carbonate reservoir deposited during the Aptian in the Alagoas Stage. This formation, characterized by its lacustrine origin, features diverse carbonate textures, including fascicular calcite crystals, calcite spherulites, and mud. Notably, microbialites are rare and mainly found in the uppermost 20-30 meters of formation. In more distal regions, shales and mudstones are predominant (Vital et al., 2023).

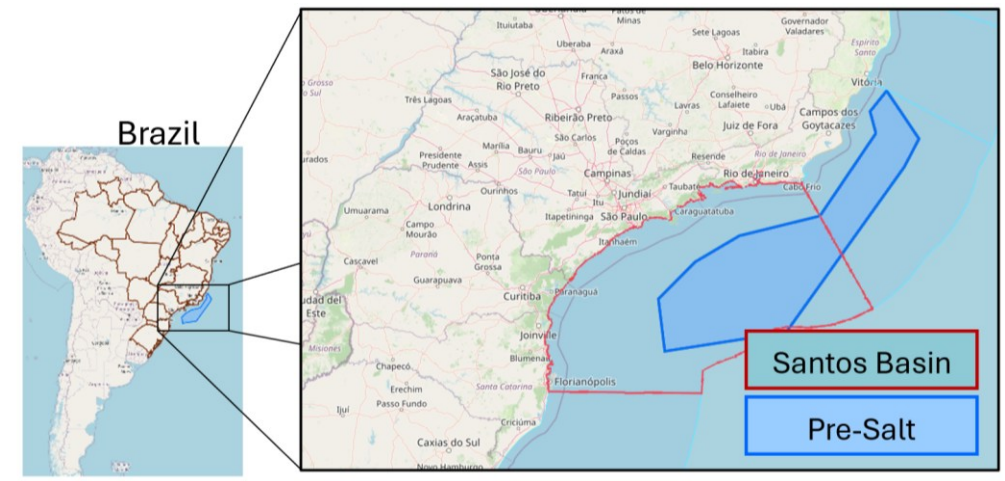

Figure 1. Santos Basin in the Brazilian pre-salt. Font: Veiga et al. (2024).

Geological samples of the Crato Formation

In the literature, it is possible to identify articles that use laminated limestones from the Crato Formation as analogs for the low-permeability calcareous facies of the reservoir rocks in the Barra Velha Formation. This is due to the correspondence in depositional age and similarities in lithology, petrophysical properties, and geomechanical characteristics. For example, Soares et al. (2015) studied hundreds of carbonate rock samples extracted from outcrops in several sedimentary basins of Northeastern Brazil and Western Portugal. The study reported values for grain density, total density, porosity, permeability, elastic properties (P and S wave velocities), and dynamic elastic moduli calculated from elastic wave velocities and total density. The results obtained in this study are vital for making estimates under any saturation condition, which would be particularly useful to support any exploration and reservoir studies. In addition, Santos et al. (2015) assessed the uncertainty due to sampling biases in scanline data of opening-mode fractures in Aptian laminated limestone outcrops from the Crato Formation. The Monte Carlo method introduced random values into sampled data to evaluate fracture network representation accuracy errors. In their analysis, errors and uncertainties were merged into a single parameter called the coefficient of uncertainty, defined as the ratio between the artificially introduced uncertainties and the original scanline data. The propagation of these errors to the power law coefficients was also analyzed. Their evaluation assists in developing more accurate geomechanical models by utilizing analog geological models for naturally fractured reservoirs. This assessment contributes to developing more precise geomechanical models by employing analog geological models for naturally fractured reservoirs. Finally, Miranda et al. (2018) investigated the fracture networks of Aptian-Albian lacustrine laminites from the Crato Formation as analogs for pre-salt carbonate facies. Traditional scanline methods characterized fractures by spacing, aperture distribution, length, and intensity. The fractures, primarily shear and extensional, exhibited a linear relationship between length and aperture, with Set 1 (NNW-SSE) and Set 2 (NE-SW) showing different distribution patterns. Fractures in Set 2 were more clustered and had wider apertures. The results provided crucial fracture attributes for Discrete Fracture Network (DFN) modeling, enhancing fluid flow simulations in carbonate reservoirs.

The Crato Formation (Figure 2), located in northeastern Brazil, is a significant lithostratigraphic unit renowned for its fossiliferous laminated limestones. Fossils in the Crato Formation encompass a variety of aquatic insect groups, providing valuable insights into both local and transported species. These fossils reveal a diverse assemblage of organisms, reflecting both native inhabitants of the ancient lake and those carried in from other aquatic environments. This formation was deposited during the Upper Aptian of the Lower Cretaceous in a large lacustrine environment, approximately 100 km by 50 km. The depositional setting included a stratified water column with well-oxygenated upper layers and anoxic lower layers, reflecting a complex paleoenvironment with varied aquatic conditions (Carvalho et al., 2023; Bezerra & Mendes, 2024; Nel & Ribeiro, 2024; Silva et al., 2024). The Crato Formation is part of the Santana Group, including the Barbalha, Ipubi, and Romualdo Formations. It features six carbonate units (C1–C6), interspersed with sandstones, siltstones, and shales. These carbonate packages are exposed in the Araripe Plateau across Ceará, Pernambuco, and Piauí, often found in commercial quarries and river margins (Storari et al., 2021).

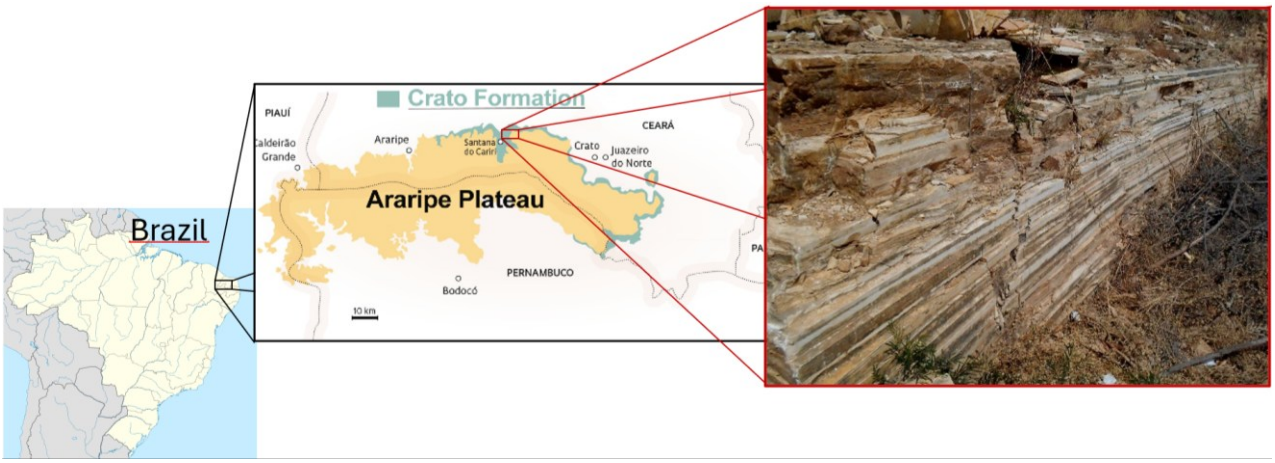

Figure 2. Crato Formation. Font: Veiga et al. (2024).

The study employed eight laminated limestone samples (Figure 3) (Table 1) from the Crato Formation. All samples have diameters ranging from 1.28 to 1.49 inches and heights between 1.60 inches and 3.67 inches. These samples are as similar to each other as natural materials allow, except for their cutting orientation. Four laminated limestone plugs from the Crato Formation were cut with their longitudinal axis perpendicular to the laminations. In contrast, the remaining four plugs were cut with their longitudinal axis parallel to the laminations.

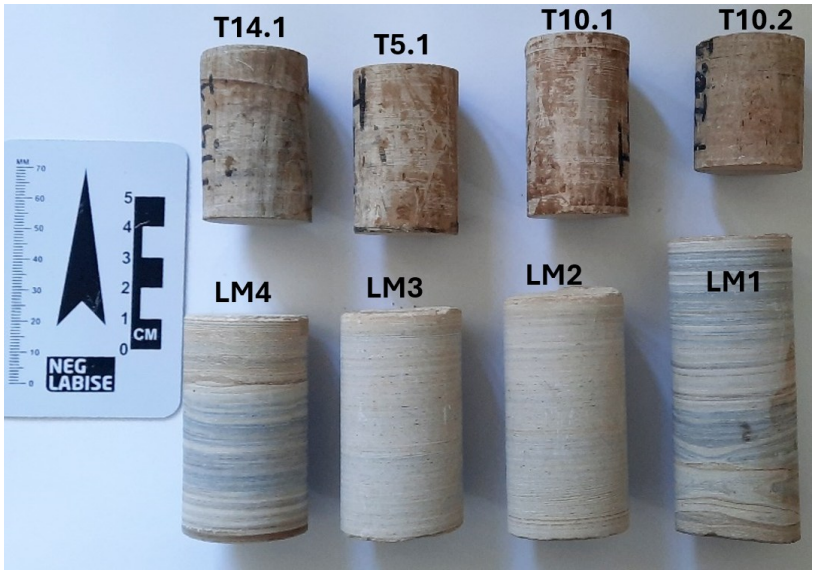

Figure 3. Laminated limestone samples from the Crato Formation. Font: Veiga et al. (2024).

Table 1. Laminated limestones samples geometrical properties. Font: Veiga et al. (2024).

Sample	Diameter ±SD (inch)	Heights ±SD (inch)	Mass (grams)
LM1	1.4912 ±0.0031	3.6734 ±0.0096	254.35
LM2	1.4890 ±0.0013	2.9444 ±0.0279	185.36
LM3	1.4866 ±0.0010	2.6682 ±0.0113	168.93
LM4	1.4926 ±0.0021	2.6202 ±0.0089	166.69
T14.1	1.3258 ±0.0019	2.0790 ±0.0018	105.11
T5.1	1.3146 ±0.0058	2.0594 ±0.0060	112.71
T10.1	1.2848 ±0.0118	2.2104 ±0.0029	109.98
T10.2	1.3268 ±0.0058	1.6030 ±0.0038	82.47

Gas Porosimetry

Porosity analyses of the eight laminated limestone samples from the Crato Formation were conducted using the gas expansion porosimetry technique at the Petrophysics Laboratory of the Departamento de Energia Nuclear of the Universidade Federal de Pernambuco (DEN-UFPE). Considering these analyses, the DCI Test Systems Helium Porosimeter (Figure 4) was employed (DCI Test Systems, n.d.). This instrument measures the pore volume of the sample through the isothermal expansion of helium gas, utilizing the principles of Boyle's and Charles's laws. The experiment was conducted at a reference pressure of approximately 100 psi. Helium was selected for its inert nature and small atomic size, ensuring accurate measurements by penetrating the sample's smallest pores. The porosity of each core plug was measured five times using the gas porosimeter, and the average of these measurements was reported.

Figure 4. Helium Porosimeter at the Petrophysics Laboratory of the DEN-UFPE. Font: Veiga et al. (2024).

X-Ray Computed Tomography

The XR-μCT studies were conducted at the X-ray Computed Tomography Laboratory (LTC-

RX) of the Porous Media Imaging, Characterization, and Simulation Research Group (ICSMP) at the DEN-UFPE. This facility has a third-generation NIKON XTH 225 ST tomography machine (Figure 5). The device operates with a maximum beam voltage of 225 kV and a maximum current of 2000 µA. It features a rectangular flat panel detector with 1520 pixels vertically and 1900 pixels horizontally, allowing for image resolutions up to 5 µm for millimeter-scale samples and several tens of micrometers for centimeter-scale objects. For cylindrical plugs with a diameter of 3.80 cm (1.5 inches) and heights ranging from 3 to 10 cm, imaging is performed at a resolution of 40 µm. The equipment also includes a variety of physical filters (Al, Cu, Sn, and Ag) with different thicknesses.

Figure 5. X-ray Computed Tomography Scanner at the DEN-UFPE. Font: Veiga et al. (2024).

The samples were positioned inside the tomography scanner and irradiated under the same conditions and pre-selected parameters (Table 2). These conditions and parameters were chosen to achieve the highest-quality tomographic images for the laminated limestone plugs, enhancing the contrast between voids and solids. The selection was based on previous experience with carbonate rock scans. Figure 6 presents a simplified diagram of the steps involved in the rock characterization method using X-ray computed tomography developed in this study.

Table 2. Experimental parameters used in the scans. Font: Veiga et al. (2024).

Parameter	Value
Current (µA)	110
Voltage (kV)	180
Filter (mm)	Cooper (0.50)
Voxel size (µm^3)	40
Integration Time (ms)	500

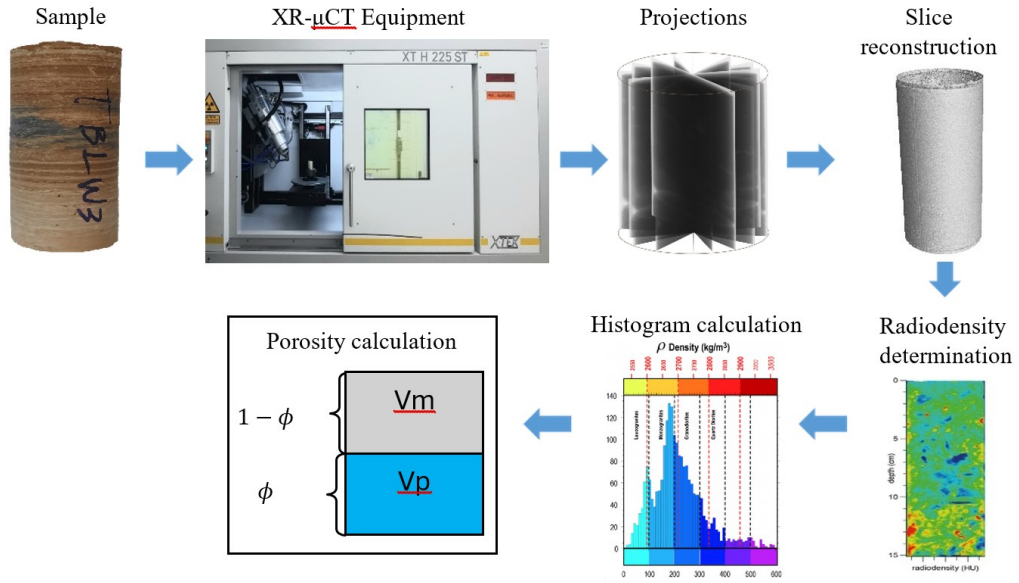

Figure 6. Flowchart for porosity calculation using XR-µCT. Font: Veiga et al. (2024).

Once the samples were scanned with a voltage higher than 100 kV, where the Compton Effect predominates, the linear attenuation coefficient of the obtained images is proportional to the density of the studied material.

Due to scattering radiation and despite using an aluminum filter, it is impossible to assert that all incident photons have energy above 100 kV. However, the sample is an attenuator; its outer layer attenuates the beam more than the interior. Only the most energetic photons can penetrate the sample's center, causing disproportionate attenuation in the outer layer. This phenomenon is known as the edge effect and is a known artifact in tomographic images (Fox et al., 2018; Ketcham & Carlson, 2001; Taguchi & Khaled, 2009; Korpics et al., 2016).

To minimize this artifact, the edges of the generated volume must be discarded during the analysis process, which was adopted for all analyzed volumes. Employing the software VGStudio MAX version 3.4 (Volume Graphics GmbH, 2020), the images were converted to Hounsfield units (Hu), where the air has a value of 0, and water has a value of 1000 (with each unit representing a 0.1% change in density).

Mathematical modeling

Traditional methods for analyzing tomographic images involve a segmentation step to distinguish between the solid matrix and the porous space. However, this approach can be problematic in samples with a smaller porosity than the pixel size, as with the studied lithology, which contains pores less than 10 μm or nanometric. Such fine details cannot be accurately captured with standard voxel resolutions, such as 40 μm^3.

An alternative method that does not rely on segmentation uses attenuation values of minerals to compare radiodensities. To achieve this, it is necessary to compare the attenuation of the studied rock with that of a known control mineral. By understanding the linear attenuation coefficient of the rock's minerals, one can infer that the difference between the expected attenuation of the mineral matrix and the observed attenuation is proportional to the void volume within each pixel. Considering rocks with a homogeneous composition, porosity can be directly derived from the image histogram, where higher radiodensity values correspond to the mineral matrix.

It is important to highlight that this method requires careful calibration of mineral attenuation and consideration of the X-ray source's polychromatic nature. Its accuracy can be affected by image artifacts, unknown mineralogy, sample heterogeneities, and variations in the X-ray energy spectrum, as the linear attenuation coefficient changes with photon energy (Ketcham & Carlson, 2001).

Calcite ($CaCO_3$), with a density of 2.71 g cm^{-3}, was chosen as the calibration mineral due to its significant presence in the matrix of carbonate rocks of interest and its role as the main constituent in the studied analogs (Heimhofer et al., 2010). A translucent, prismatically shaped calcite sample, approximately 6 x 3 x 1 cm, was scanned to obtain the average attenuation. As with the rock samples, the edges of the calcite sample were excluded to mitigate the influence of the edge effect caused by beam hardening. Despite the sample's relatively homogeneous composition, it exhibits structural heterogeneities such as porosity, fractures, diagenetic variations, and other micro- or nanometric imperfections. To reduce uncertainty in determining a representative attenuation value for the mineral, a normal distribution was applied to the average attenuation values of the slices. Based on the normal distribution, the mineral matrix of the samples was represented by slices with the highest attenuation values. The threshold was set at a point corresponding to the 95th percentile of the normal distribution. This value is the attenuation caused by a solid voxel with a material of 2.71 $g{\cdot}cm^{-3}$ density and homogeneous composition under standard acquisition and processing conditions. Values below this threshold are considered mixed voxels, meaning they contain both mineral matrix and pores.

Equation 1 can be used to determine the density of a given voxel in the rock samples. This method allows for measuring density at discrete points or volumes of interest within the object. This property was used in this study to check for any correlation between the laminations and the density distribution in the rock.

$$\rho\left[\frac{g}{cm^3}\right] = \frac{\mu[Hu]}{\psi} \qquad \text{Eq. (1)}$$

where ψ is the calibration coefficient and follows the form of Equation 2. The value of ψ was obtained by the ratio between the attenuation of the calibration mineral (obtained from the $CaCO_3$ scans) and its theoretical density.

$$\psi = \frac{\mu_{mineral}}{\rho} \qquad \text{Eq. (2)}$$

Similarly, the porosity can be estimated as a ratio of the attenuation coefficients of the calibration mineral and the rock samples (Equation 3).

$$Porosity\ [\%] = \frac{\mu_{mineral} - \mu_{rock\ sample}}{\mu_{mineral}} \quad \text{Eq. (3)}$$

Results and Discussion

Gas porosimeter results

Table 3 shows the results of the porosity analysis for the eight laminated limestone samples from the Crato Formation using the gas expansion porosimetry technique. The values presented in Table 3 represent the samples' effective porosity (P_{He}), meaning the fraction of interconnected voids within the rock volume that allows the passage of the gas used in the experiment. These results indicate a notable range in porosity values, from a low of 8.54% in sample T5.1 to a high of 19.05% in sample LM4.

Table 3. Porosity analysis using the gas porosimetry technique. Font: Veiga et al. (2024).

Sample	P_{He} (%)
LM1	12.28 ±0.13
LM2	17.68 ±0.30
LM3	17.48 ±0.26
LM4	19.05 ±0.30
T14.1	17.60 ±0.29
T5.1	8.54 ±0.35
T10.1	13.12 ±0.13
T10.2	16.04 ±0.46

This variation indicates the heterogeneous nature of the laminated limestones, which is a critical factor in assessing the potential of these formations as hydrocarbon reservoirs. The relatively higher porosity values in samples LM2, LM3, LM4, and T14.1 (above 17%) suggest more extensive void networks, likely enhancing fluid flow within these rocks.

These samples could represent zones within the formation where depositional conditions favored the development of larger or more interconnected pore spaces. Conversely, the lower porosity in samples T5.1, LM1, and T10.1, at 8.54%, 12.28%, and 13.12%, respectively, points to tighter rock fabrics. These samples might correspond to areas within the formation where depositional or post-depositional processes, such as compaction or cementation, have reduced pore space. These differences could significantly impact the overall permeability and, consequently, the extractability of fluids from these rocks.

Evaluation of the traditional threshold-based method for porosity estimation

An initial study was conducted using one of the samples, T14.1, which had shown one of the highest porosity values (17.60%) in the gas porosimetry analysis. This sample was selected to evaluate the effectiveness of the traditional threshold-based method for porosity estimation. The method was applied to the tomographic images of T14.1 to assess how well it could detect porosity at this scale.

The results revealed that the traditional threshold-based method only detected a porosity of 0.45%, far below the gas porosimetry result. This discrepancy highlights the limitations of the threshold-based approach when the pore sizes are below the resolution of the tomography scanner. These results underscore the challenges of fine-scale porosity in samples like T14.1, where the scanner does not capture much of the pore space. Figure 7 illustrates the spatial distribution of the detected pores in a 3D image obtained during the threshold analysis, further emphasizing the method's inability to detect smaller pores effectively.

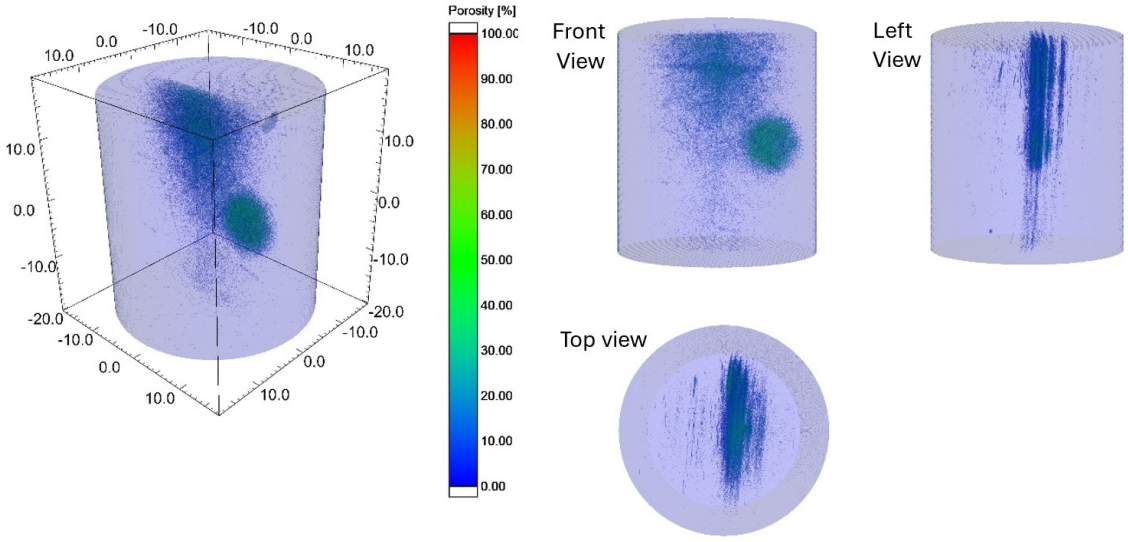

Figure 7. Average attenuation values for each slice of the calcite sample. Font: Veiga et al. (2024).

Calcite calibration results

Calcite calibration is critical in establishing the appropriate calibration parameter for the analyzed rocks, specifically calcite with a 2.71 g cm^{-3} density. This mineral, identified as the principal component of the rock samples in previous studies (Heimhofer et al., 2010; Gurjão et al., 2013; Soares et al., 2015), plays a crucial role in our analysis.

The calibration process is essential to ensure the accuracy of our porosity and density measurements, allowing for refined interpretations of the imaging data. Figure 8 shows the average attenuation values (in Hounsfield units) for the calcite sample after μCT scanning; the edges of the calcite sample were excluded. Figure 9 shows the normal distribution applied to the average attenuation values of the slices to reduce the uncertainty in determining the representative attenuation value for the mineral.

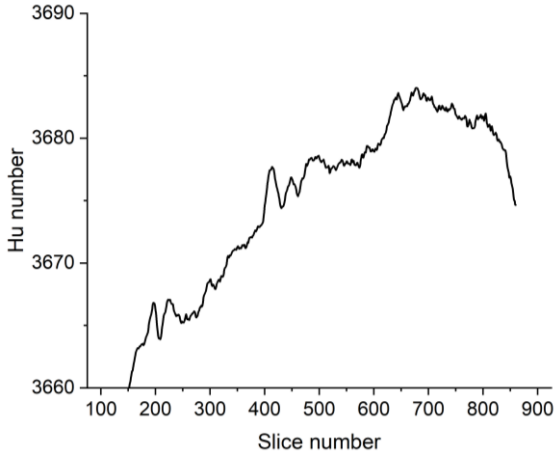

Figure 8. Average attenuation values for each slice of the calcite sample. Font: Veiga et al. (2024).

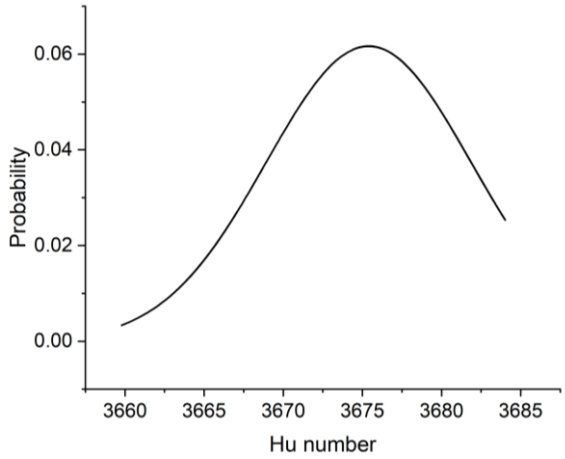

Figure 9. Normal distribution of the average attenuation values of the slices of the calcite sample. Font: Veiga et al. (2024).

Following the methodology outlined in Section 2.4, the attenuation threshold, a point greater than 95% of the normal distribution, was established at 3686.04 Hu. This value reflects the attenuation characteristic of a solid calcite volume with a density of 2.71 g·cm^{-3} and uniform composition under standard acquisition and processing conditions. When applied to Equation 2, the calculation yielded a ψ value of 1360.16, which is representative of the intrinsic properties of calcite. Subsequently, by applying this calibration coefficient, it is possible to reformulate the curve in Figure 9 in terms of density. As illustrated in Figure 10, the recalibrated average densities are approximately 2.705 g·cm^{-3}. Similarly, applying the calibration coefficient to the data presented in Figure 8 yields the density distribution for all slices of the calcite sample (Figure 11). The values obtained after calibration confirm that, despite the calcite sample exhibiting structural heterogeneities such as porosity, fractures, diagenetic variations, and other micro- or nanometric imperfections, its density values are consistent with those reported in the literature for this material.

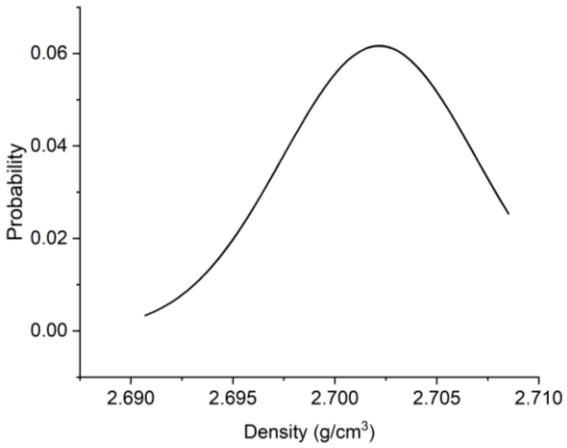

Figure 10. Normalized curve for the density distribution of the calcite sample. Font: Veiga et al. (2024).

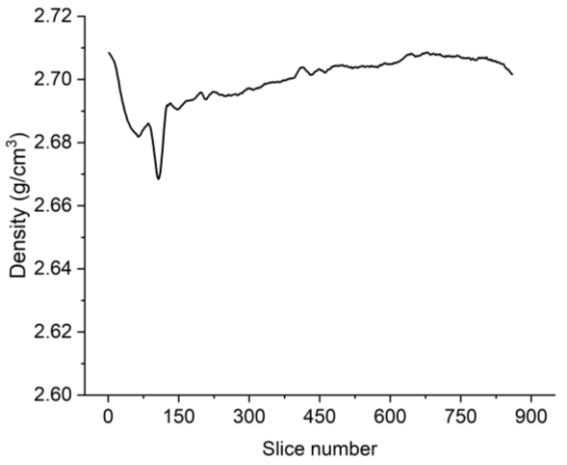

Figure 11. Density distribution in the slices of the calcite sample. Font: Veiga et al. (2024).

Obtaining physical indices of rock samples from tomographic images

Following the establishment of the calibration for the mineral of interest, eight samples of laminated limestones from the Crato Formation were analyzed. As previously described in the methodology, the volumes selected for analysis, taken from the interior of the samples, were reconstructed in Hounsfield units. The average attenuation value of the selected region from each slice was plotted in the charts in Figure 12. Next, the calibration coefficient (ψ) was applied to the values in the graphs from Figure 12, resulting in the graph shown in Figure 13.

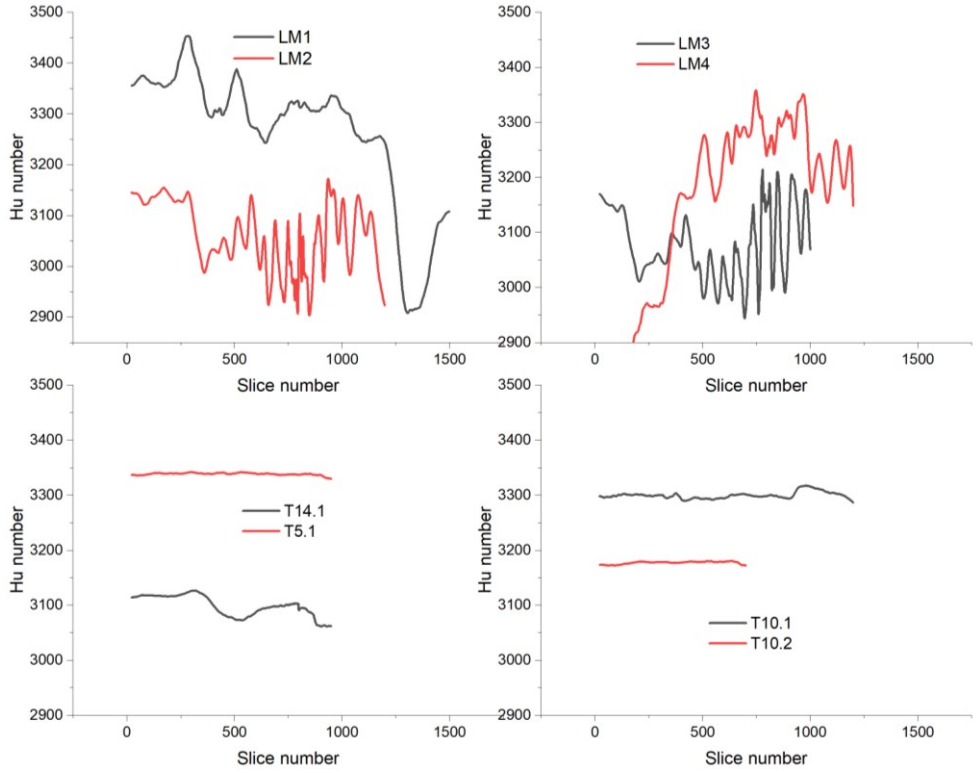

Figure 12. Average attenuation of each slice of the selected sample volume. Font: Veiga et al. (2024).

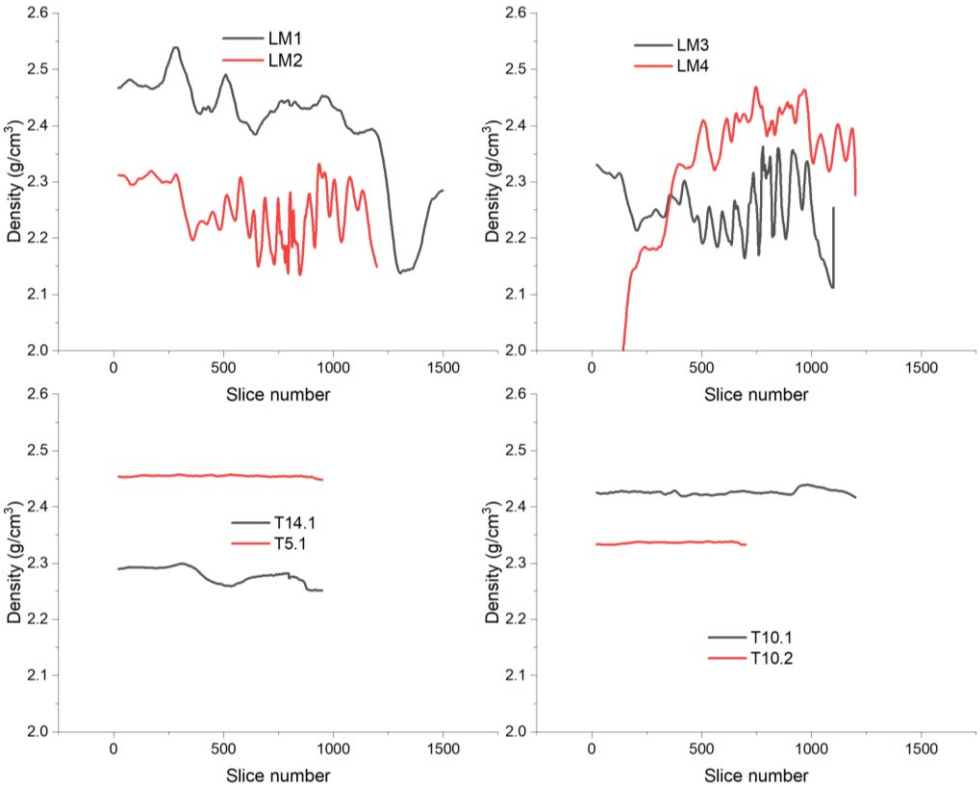

Figure 13. Density distribution in the slices of the laminated limestone samples. Font: Veiga et al. (2024).

The profiles reveal distinct variations across the samples, distinguishing between those cut perpendicular and those cut parallel to the sedimentary layers. LM1 to LM4, cut perpendicular to the laminations, exhibit more significant fluctuations in HU values, particularly in LM2 and LM3. This suggests a higher degree of heterogeneity in these samples, likely due to slicing through multiple sedimentary layers with varying compositions. In contrast, the other four samples (T14.1, T5.1, T10.1, and T10.2), which were cut parallel to the laminations, display relatively stable attenuation profiles, reflecting more consistent material properties along the plane of the laminations.

Figure 13 presents the corresponding density profiles, where the general trends mirror the attenuation data. Samples LM2 and LM3 show greater variability in density, likely due to the heterogeneity between sedimentary layers, while T14.1, T5.1, T10.1, and T10.2, with their more uniform laminations, show much more stable density profiles across the slices. These results highlight how cutting orientation relative to the sedimentary layers affects both attenuation and density measurements, with more variability observed when the sample is cut across the laminations. The comparison of density profiles across the samples reveals a broad spectrum of material properties, from dense, compacted rocks to more porous, less dense structures. The higher densities observed in LM1 and LM4 suggest rocks with lower porosity and potentially greater mechanical strength. In comparison, the lower densities in T14.1 and T10.2 indicate rocks that may be more porous and have a higher potential for fluid storage. T5.1 and LM2 serve as intermediate cases, suggesting a balance between compaction and porosity, making them less extreme but still informative for understanding the overall characteristics of the Crato Formation.

The next step was the determination of porosities, for which Equation 3 was used. This equation compared the measured attenuation, specifically the average attenuation of a given slice, with the attenuation of the calibration mineral. Areas with radiodensity higher than the calibration mineral were estimated to have 0% porosity, while for the remaining areas, porosity values between 0 and 100% were assigned according to Equation 3. Figure 14 compares the porosity distribution of the studied samples, and Table 4 shows the average porosity values, along with a comparison to the values obtained through gas porosimetry.

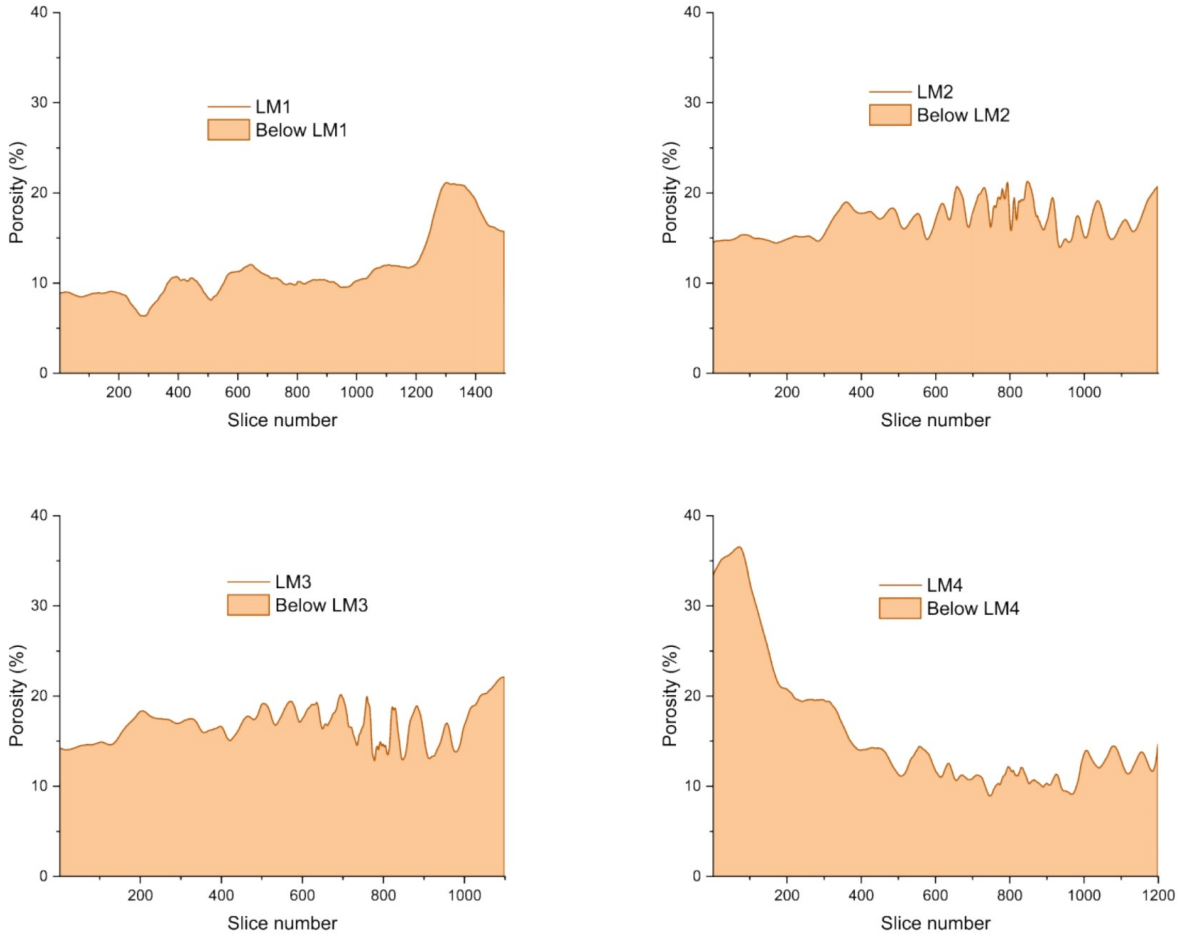

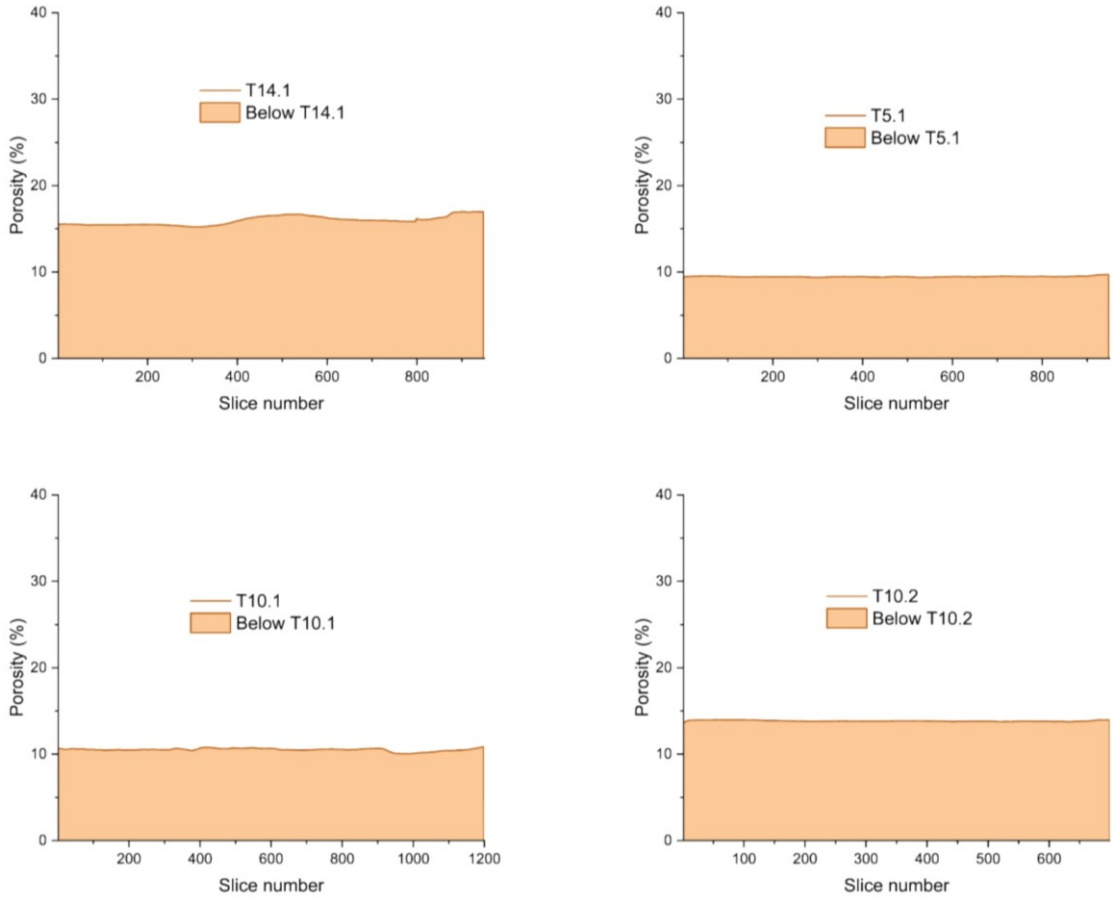

Figure 14. Porosity distribution in the slices of the laminated limestone samples. Font: Veiga et al. (2024).

Table 4. Comparison of the porosity results using the XR-µCT and gas porosimetry technique. Font: Veiga et al. (2024).

Sample	XR-µCT (%)	P_{He} (%)	Relative difference (%)
LM1	13.45	12.28	9.50
LM2	17.32	17.68	-2.00
LM3	16.81	17.48	-3.80
LM4	16.02	19.05	-15.90
T14.1	15.98	17.60	-9.20
T5.1	9.46	8.54	10.70
T10.1	11.91	13.12	-9.20
T10.2	13.99	16.04	-12.80

Figure 14 shows the average porosity distribution obtained from XR-µCT for each slice of the laminated limestone samples. The distribution highlights the variation in porosity across the samples, with noticeable differences in the porosity values within and between the samples. Samples LM1 and LM4 exhibit more heterogeneous porosity distribution, with fluctuations in the porosity across different slices, suggesting that these samples may have more internal variability, possibly due to differences in depositional layers or post-depositional alterations. On the other hand, samples T14.1, T5.1, T10.1, and T10.2 display more consistent porosity profiles, which can be attributed to the fact that these samples were cut parallel to the laminations. In this orientation, multiple sedimentary layers are averaged together in each slice, resulting in a more homogenized representation of porosity. The XR-µCT technique, which calculates the average attenuation per slice, further smooths out local variations within individual layers, contributing to the apparent uniformity in the profiles. This effect is less pronounced in samples cut perpendicular to the laminations, where distinct layers are more clearly resolved, leading to greater variability in the porosity profiles.

In Table 4, a comparison between the porosity results obtained from XR-µCT and the gas porosimetry technique is presented. The porosity values from both methods align relatively well, with most samples showing a relative difference

within 10%, except for LM4 and T10.2, where the relative difference reaches -15.9% and -12.8%, respectively. These discrepancies could be attributed to how the two methods manage pore connectivity and pore size distribution. Gas porosimetry measures effective porosity, focusing on interconnected pore spaces, whereas XR-μCT captures the total porosity, including isolated pores that do not contribute to gas flow. This difference in methodology likely explains the higher porosity values observed for LM4 and T10.2. Finally, it is important to highlight that the results obtained for both density and porosity fall within the range of values reported in the literature for the analyzed region (Heimhofer et al., 2010; Gurjão et al., 2013; Soares et al., 2015).

Conclusion

X-ray computed microtomography successfully estimated the porosity and density in laminated limestones from the Crato Formation, providing valuable insights into their potential as reservoir analogs. The results confirmed that when properly calibrated using a calcite sample, the applied method can yield reliable estimates that closely align with traditional gas porosimetry. However, the threshold-based method, applied to one of the samples (T14.1), revealed significant limitations, detecting only 0.45% porosity, far below the 17.60% measured by gas porosimetry, thus highlighting the challenges of capturing pores below the scanner's resolution.

This study emphasized the crucial role of calibration in XR-μCT analysis, particularly in complex sedimentary systems, where heterogeneities can greatly influence porosity and density distributions. Samples cut parallel to sedimentary laminations exhibited more consistent porosity profiles, further validating the method's ability to analyze heterogeneous rock structures. Overall, this study reinforces the potential of XR-μCT as a non-invasive tool for reservoir characterization, contributing to more accurate geological and environmental models.

Acknowledgments

This research was partially supported by the Fundação de Amparo à Ciência e Tecnologia do Estado de Pernambuco (FACEPE), project number BFP-0146-3.09/23, the Human Resources Program of the Agência Nacional do Petróleo, Gás Natural e Biocombustíveis (ANP) PRH 48.1 "Characterization and Simulation of Reservoirs, Renewable Energy and Environmental Biotechnology", and the Conselho Nacional de Desenvolvimento Científico e Tecnológico (CNPq), Project Number 465764/2014-2 - Observatório Nacional da Dinâmica da Água e de Carbono no Bioma Caatinga (ONDACBC). The authors also acknowledge CNPq for research support, including the Junior Postdoctoral Fellowship awarded to Abel Gámez Rodríguez (Process No. 174032/2023-4) and the Productivity Fellowship granted to Antonio Celso Dantas Antonino.

References

Abelha M.; Petersohn E. 2019. The State of the Art of the Brazilian Pre-Salt Exploration. AAPG Prospect and Property Expo. Available at: https://www.gov.br/anp/pt-br/centrais-de-conteudo/apresentacoes-palestras/2019/arquivos/2019/abelha_marina_brazilian-pre-salt_appex_2019mar6.pdf

Alencar, M. L.; Miranda, T. S.; Correia Filho, O. J.; Barbosa, J. A.; Gomes, I. F.; Ramos, G. M. S.; Araújo, A. F. L.; Topan, J. G. de O.; Celestino, M. A. L.; Neumann, V. H. 2024. The effect of fracture networks on the vertical permeability of a tight carbonate reservoir analogue: laminites from the Crato Formation, NE Brazil. Marine and Petroleum Geology, 162, 106735. https://doi.org/10.1016/j.marpetgeo.2024.106735

Bezerra, F. I.; Mendes, M. 2024. A palaeoecological analysis of the Cretaceous (Aptian) insect fauna of the Crato Formation, Brazil. Palaeogeography, Palaeoclimatology, Palaeoecology, 641, 112134. https://doi.org/10.1016/j.palaeo.2024.112134

Busch, B.; Spitzner, A. D.; Adelmann, D.; Hilgers, C. 2022. The significance of outcrop analog data for reservoir quality assessment: A comparative case study of Lower Triassic Buntsandstein sandstones in the Upper Rhine Graben. Marine and Petroleum Geology, 141, 105701. https://doi.org/10.1016/j.marpetgeo.2022.105701

Cnudde, V.; Boone, M. N. 2013. High-resolution X-ray computed tomography in geosciences: A review of the current technology and applications. Earth-Science Reviews, 123, 1-17. https://doi.org/10.1016/j.earscirev.2013.04.003

Silva, V. R.; Varejão, F. G.; Matos, S. A.; Rodrigues, M. G.; Warren, L. V.; Assine, M. L.; Fürsich, F. T.; Simões, M. G. 2024. A new condensed freshwater-brackish water bivalve-dominated assemblage in the Aptian Crato Formation, Araripe Basin, NE Brazil and its paleoenvironmental significance.

Cretaceous Research, 154, 105748. https://doi.org/10.1016/j.cretres.2023.105748

DCI Test Systems. Helium Porosimeter. Available at: https://www.dcitestsystems.com/helium-porosimeter.html. Access at: 01/09/2024.

Carvalho, M. G. P.; Maisey, J. G.; Mendes, I. D.; Souza C. I. 2023. Micro-tomographic analysis of a scorpion fossil from the Aptian Crato Formation of Northeastern Brazil. Cretaceous Research, 147, 105454. https://doi.org/10.1016/j.cretres.2022.105454

Dou, L.; Wen, Z.; Wang, Z.; He, Z.; Song, C.; Chen, R.; Yang, X.; Liu, X.; Liu, Z.; Chen, Y. 2024. Sedimentary build-ups of pre-salt isolated carbonate platforms and formation of deep-water giant oil fields in Santos Basin, Brazil. Petroleum Exploration and Development, 51, (4), 949-962. https://doi.org/10.1016/S1876-3804(24)60517-3

Fox, A.; Basrani, B.; Kishen, A.; Lam, E. W. N. 2018. A Novel Method for Characterizing Beam Hardening Artifacts in Cone-beam Computed Tomographic Images. Journal of Endodontics, 44, (5), 869-874. https://doi.org/10.1016/j.joen.2018.02.005

Gurjão, K. G. R.; Soares, J. A.; Figueiredo, A. N. 2013. Petrophysics of carbonatic and evaporitic rocks from Araripe Basin. 13th International Congress of the Brazilian Geophysical Society, Rio de Janeiro, Brazil. https://doi.org/10.1190/sbgf2013-235

Hai, W.; Xue, Q.; Wang, M.; He, Y. 2024. Parameter optimization based on deepwater drilling system simulation: A pre-salt exploration well in Brazil. Geoenergy Science and Engineering, 241, 213120. https://doi.org/10.1016/j.geoen.2024.213120

Heimhofer, U.; Ariztegui, D.; Lenniger, M.; Hesselbo, S. P.; Martill, D. M.; Rios-Netto, A. M. 2010. Deciphering the depositional environment of the laminated Crato fossil beds (Early Cretaceous, Araripe Basin, North-eastern Brazil). Sedimentology, 57, (2), 677-694. https://doi.org/10.1111/j.1365-3091.2009.01114.x

Herlinger, R.; Vidal, A. C. 2022. X-ray μCt extracted pore attributes to predict and understand Sor using ensemble learning techniques in the Barra Velha Pre-salt carbonates, Santos Basin, Offshore Brazil. Journal of Petroleum Science and Engineering, 212, 110282. https://doi.org/10.1016/j.petrol.2022.110282

Islam, A.; Chevalier, S.; Sassi, M. 2018. Structural characterization and numerical simulations of flow properties of standard and reservoir carbonate rocks using micro-tomography. Computers & Geosciences, 113, 14-22. https://doi.org/10.1016/j.cageo.2018.01.008

Neves Junior, A.; Queiroz, G. N.; Godoy, M. G.; Cardoso, V. S.; Cedrola, S. M. L.; Mansoldo, F. R. P.; Firpo, R. M.; Paiva, L. M.; Sohrabi, M.; Vermelho, A. B. 2023. Assessing EOR strategies for application in Brazilian pre-salt reservoirs. Geoenergy Science and Engineering, 223, 211508. https://doi.org/10.1016/j.geoen.2023.211508

Kadyrov, R.; Statsenko, E.; Nguyen, T. H. 2024. Integrating μCT imaging of core plugs and transfer learning for automated reservoir rock characterization and tomofacies identification. Marine and Petroleum Geology, 168, 107014. https://doi.org/10.1016/j.marpetgeo.2024.107014

Ketcham, R. A.; Carlson, W. D. 2001. Acquisition, optimization and interpretation of X-ray computed tomographic imagery: applications to the geosciences. Computers & Geosciences, 27, (4), 381-400. https://doi.org/10.1016/S0098-3004(00)00116-3

Korpics, M.; Surucu, M.; Mescioglu, I.; Alite, F.; Block, A. M.; Choi, M.; Emami, B.; Harkenrider, M. M.; Solanki, A. A.; Roeske, J. C. 2016. Observer Evaluation of a Metal Artifact Reduction Algorithm Applied to Head and Neck Cone Beam Computed Tomographic Images. International Journal of Radiation Oncology, Biology, Physics, 96, (4), 897-904. https://doi.org/10.1016/j.ijrobp.2016.07.028

Liu, C.; Buono, G.; Pappalardo, L.; Shan, X.; Yi, J.; Shi, Y.; Ventura, G. 2023. X-ray computed microtomography revealing the effects of volcanic, alteration, and burial processes on the pore structure of rocks from unconventional reservoirs (Songliao Basin, NE China). Geoenergy Science and Engineering, 226, 211781. https://doi.org/10.1016/j.geoen.2023.211781

Liu, Q.; Sun, M.; Sun, X.; Liu, B.; Ostadhassan, M.; Huang, W.; Chen, X.; Pan, Z. 2023. Pore network characterization of shale reservoirs through state-of-the-art X-ray computed tomography: A review. Gas Science and Engineering, 113, 204967. https://doi.org/10.1016/j.jgsce.2023.204967

Lv, J.; Zhao, J.; Jiang, L.; Liu, Y.; Mu, H. 2020. A review of micro computed tomography studies on the gas hydrate pore habits and seepage properties in hydrate bearing sediments. Journal of Natural Gas Science

and Engineering, 83, 103555. https://doi.org/10.1016/j.jngse.2020.103555

Martyushev, D. A.; Ponomareva, I. N.; Chukhlov, A. S.; Davoodi, S.; Osovetsky, B. M.; Kazymov, K. P.; Yang, Y. 2023. Study of void space structure and its influence on carbonate reservoir properties: X-ray microtomography, electron microscopy, and well testing. Marine and Petroleum Geology, 151, 106192. https://doi.org/10.1016/j.marpetgeo.2023.106192

Michael, A. 2024. Transparent gelatin as a reservoir analogue: Dimensional scaling for hydraulic fracturing laboratory experiments. International Journal of Rock Mechanics and Mining Sciences, 177, 105732. https://doi.org/10.1016/j.ijrmms.2024.105732

Miranda, T. S.; Santos, R. F.; Barbosa, J. A.; Gomes, I. F.; Alencar, M. L.; Correia, O. J.; Falcão, T. C.; Gale, J. F. W.; Neumann, V. H. 2018. Quantifying aperture, spacing and fracture intensity in a carbonate reservoir analogue: Crato Formation, NE Brazil. Marine and Petroleum Geology, 97, 556-567. https://doi.org/10.1016/j.marpetgeo.2018.07.019

Nel, A.; Ribeiro, G. C. 2024. New fossil wings shed light on Lower Cretaceous Araripechlorogomphidae and minimum age of the Chlorogomphoidea (Odonata: Anisoptera): Crato formation, Araripe Basin, NE Brazil. Cretaceous Research, 156, 105811. https://doi.org/10.1016/j.cretres.2023.105811

Pak, T.; Archilha, N. L.; Berg, S.; Butler, I. B. 2023. Design considerations for dynamic fluid flow in porous media experiments using X-ray computed micro tomography – A review. Tomography of Materials and Structures, 3, 100017. https://doi.org/10.1016/j.tmater.2023.100017

Pilotto, D.; Zanella, R.; Magnavita, L.; Stanton, N.; Oliveira, J. P.; Borghi, L. 2024. The Espadarte transfer zone: Structural architecture and kinematics of an oblique basement high controlling pre-salt geometry in south Campos basin, SE Brazil. Journal of South American Earth Sciences, 143, 105012. https://doi.org/10.1016/j.jsames.2024.105012

Rossoni, R. B.; Porcher, C. C.; Koester, E.; Sobiesiak, J. S.; Silva, L. A. C.; Mexias, A. S.; Gomes, M. E. B.; Ramnani, C. W.; De Ros, L. F. 2024. The role of compaction in the diagenetic evolution of Pre-Salt Aptian deposits of Santos Basin, Brazil. Sedimentary Geology, 466, 106650. https://doi.org/10.1016/j.sedgeo.2024.106650

Santos, R. F. V. C.; Miranda, T. S.; Barbosa, J. A.; Gomes, I. F.; Matos, G. C.; Gale, J. F. W.; Neumann, V. H. L. M.; Guimaraes, L. J. N. 2015. Characterization of natural fracture systems: Analysis of uncertainty effects in linear scanline results. AAPG Bulletin, 99, (12), 2203-2219. https://doi.org/10.1306/05211514104

Shukla, A.; Sahoo, S.; Sarkar, P. 2024. Assessment of micro-structure and flow entrapment in Indian Gondwana shale reservoir using digital rock analysis. Marine and Petroleum Geology, 169, 107066. https://doi.org/10.1016/j.marpetgeo.2024.107066

Soares, J. A.; Garcia, A. J. V.; Bezerra, F. H. R.; Barbosa, J. A.; Friedrich, A.; Cazarin, C. L.; Tabosa, L. D. G.; Coura, R. L. C. 2015. Petrophysics and Rockphysics of Carbonates from Brazil and Portugal. 14th International Congress of the Brazilian Geophysical Society & EXPOGEF, Rio de Janeiro, Brazil, pp. 882-887. https://doi.org/10.1190/sbgf2015-173

Storari, A. P.; Rodrigues, T.; Bantim, R. A. M.; Lima, F. J.; Saraiva, A. A. F. 2021. Mass mortality events of autochthonous faunas in a Lower Cretaceous Gondwanan Lagerstätte. Scientific Reports, 11, (1), 6976. https://doi.org/10.1038/s41598-021-85953-5

Taguchi, K.; Khaled, A. 2009. Artifacts in Cardiac Computed Tomographic Images. Journal of the American College of Radiology, 6, (8), 590-593. https://doi.org/10.1016/j.jacr.2009.05.001

Teles, A. P.; Machado, A. C.; Pepin, A.; Bize-Forest, N.; Lopes, R. T.; Lima, I. 2016. Analysis of subterranean Pre-salt carbonate reservoir by X-ray computed microtomography. Journal of Petroleum Science and Engineering, 144, 113–120. https://doi.org/10.1016/j.petrol.2016.03.008

Valencia-Gómez, J. C.; Cardona, A.; Zapata, S.; Monsalve, G.; Marín, D.; Rodríguez-Cuevas, M.; Sobel, E. R.; Parra, M.; Glodny, J. 2024. Fracture analysis and low-temperature thermochronology of faulted Jurassic igneous rocks in the Southern Colombian Andes: Reservoir and tectonic implications. Marine and Petroleum Geology, 165, 106850. https://doi.org/10.1016/j.marpetgeo.2024.106850

Vital, J. C. S.; Ade, M. V. B.; Morelatto, R.;

Lupinacci, W. M. 2023. Compartmentalization and stratigraphic-structural trapping in pre-salt carbonate reservoirs of the Santos Basin: A case study in the Iara complex. Marine and Petroleum Geology, 151, 106163. https://doi.org/10.1016/j.marpetgeo.2023.106163

Volume Graphics GmbH. 2020. VGSTUDIO MAX 3.4 Reference Manual. Available at: https://www.volumegraphics.com/en/products/vgsm.html

Wang, M.; Yang, S.; Li, J.; Zheng, Z.; Wen, J.; Ma, Q.; Wang, Q.; Chen, H. 2021. Cold water-flooding in a heterogeneous high-pour-point oil reservoir using computerized tomography scanning: Characteristics of flow channel and trapped oil distribution. Journal of Petroleum Science and Engineering, 202, 108594. https://doi.org/10.1016/j.petrol.2021.108594

Wellington, S. L.; Vinegar, H. J. 1987. X-ray computerized tomography. Journal of Petroleum Technology, 39, (8), 885-898. https://doi.org/10.1016/0308-9126(90)92264-2

Xie, L.; You, Q.; Wang, E.; Li, T.; Song, Y. 2022. Quantitative characterization of pore size and structural features in ultra-low permeability reservoirs based on X-ray computed tomography. Journal of Petroleum Science and Engineering, 208, 109733. https://doi.org/10.1016/j.petrol.2021.109733

Zhu, J. B.; Zhou, T.; Liao, Z. Y.; Sun, L.; Li, X. B.; Chen, R. 2018. Replication of internal defects and investigation of mechanical and fracture behaviour of rock using 3D printing and 3D numerical methods in combination with X-ray computerized tomography. International Journal of Rock Mechanics and Mining Sciences, 106, 198-212. https://doi.org/10.1016/j.ijrmms.2018.04.022